Stabilisation of aluminium foams and films by the joint action of dispersed particles and oxide films

K. Heim[1,2], G. S. Vinod-Kumar[2,*], F. García-Moreno[1,2], A. Rack[3], J. Banhart[1,2]

[1] Technische Universität Berlin, Hardenbergstraße. 36, 10623 Berlin, Germany

[2] Helmholtz-Zentrum Berlin für Materialien und Energie, Hahn Meitner Platz 1, 14109 Berlin, Germany

[3] European Synchrotron Radiation Facility, 71 avenue des Martyrs, 38000 Grenoble, France

* now at: SRM Research Institute, SRM University, Kattankulathur, 603203, India

Aluminium alloy foams are created by injecting gas containing different levels of oxygen (from <<1 ppm to 21%) into melts stabilised with SiC or TiB_2 particles. Individual liquid aluminium alloy films meant to represent the films in a foam are produced of the same materials. In both cases, the oxygen concentration of the atmosphere is controlled. Synchrotron X-ray radioscopy on liquid films is applied to track the movements of the particles within and to observe how they flow, pile up and form clusters. Experiments on aluminium foams show that only when the injected gas and atmosphere contains oxygen foams can be expanded continuously. In contrast, if foaming is carried out by injecting argon into the melt and the Ar atmosphere is free of oxygen no stable foams can be created, even if the melt contains 20 vol.% SiC particles. Both film and foam surfaces are analysed ex-situ by energy-filtered TEM and SEM. It is found that oxide films form, cover the particles and push them into the metal. High oxygen content in combination with Mg in the alloy promotes this process. It is concluded that not only particles are required to allow foaming, but also the formation of an oxide skin is necessary and the combination of both are the basis of film and foam stabilisation.

Keywords: Aluminium foam, single film, particle stabilised, X-ray imaging, synchrotron radioscopy

1. Introduction

The stabilisation of liquid metal foams is still only poorly understood for any of the different types of foaming processes based either on metal powders or on molten alloys [1-4]. Liquid metal foams are transient and prone to drainage, coarsening and coalescence. An investigation of the stabilising mechanisms in such liquid foams is necessary to be able to improve foaming processes and the resulting solid foam properties such as the pore size distribution and uniformity of density, and finally their mechanical parameters.

Up to now, most of the efforts to understand foam stability are based on the study of entire foams, more specifically how they expand, what the reasons for destabilisation are and how the decay of foams can be prevented [3, 5, 6]. The present authors have suggested investigating liquid foam stability by studying the simplified model system of single metal films instead [7, 8]. In aqueous systems, the comparability of the model system 'single film' and real foams has been substantiated [9, 10]. This allows one to apply a wide range of experimental methods to investigate specific effects more precisely as it would be possible for entire foams, e.g. particle movements in the liquid or a defined oxygen concentration and oxidation time.

For aluminium alloys, a certain amount of solid particles (for example in AlSi9Mg0.6 either 20 vol.% SiC or 6 vol.% TiB_2) is required to stabilise a liquid film [11], which agrees with what is known for foams created by gas injection, where particles have to be present as well [12, 13]. It comes as a new finding that also a minimum amount of oxygen, namely > 200 ppm is required [8]. This suggests that oxygen is not only important for the creation of metal foams as already known but essential.

Hitherto, the stability of aluminium foams has been investigated by analysing solidified foams by microscopy and studying the morphology and the arrangement of solid particles inside their cell walls [14, 15]. In addition, liquid foams have also been studied in-situ by means of X-ray radioscopy with an emphasis on foam expansion and decay (characterised by the coalescence rate) [16, 17]. In the present work, we combine these two approaches and demonstrate for the first time how particles behave and arrange inside an individual liquid aluminium film by using in-situ synchrotron X-ray radioscopy [18]. We foam different alloys by injecting gas containing various oxygen levels and select different surrounding atmospheres. The impact of oxygen on film stability is also investigated using energy-filtered transmission electron microscopy (EFTEM) on samples taken from the solidified inner bubble surface.

2. Experimental

2.1. Materials

Aluminium alloys containing various elements and stabilising particles are used for studying liquid film and foam stability. Three particle-free alloys are prepared: pure Al, AlSi9 and AlSi9Mg0.6. The latter is made by adding 0.6 wt.% Mg to an as-received commercial AlSi9 alloy. Three composites, each containing 6 vol.% TiB_2, are made via flux-assisted synthesis by an in-situ reaction, yielding particles of 0.5–3 µm mean diameter [19]. Moreover, a composite of AlSi9Mg0.6 containing 20 vol.% SiC particles with a mean particle size of 10 µm (F3S20S made by Alcan, Montréal, Canada) is used. Particle-free AlSi9Mg0.6 melt is used for diluting this composite to the second desired concentration of 10 vol.% SiC particles. Hence, in total 5 different composites are investigated.

2.2. Films

Single metallic films (SF) are produced in a controlled atmosphere by pulling a circular frame made of molybdenum wire out of a melt and solidifying the film created within 10 s. The oxygen content of the surrounding atmosphere is adjusted in the range from $\ll$1 ppm to 21% O_2 to study its influence on film stability. The setup is sketched in Figure 1a). A description of the film pulling process can be found elsewhere [8]. The shape of the wire frame and the structure of the corresponding film are further modified to more complex quadruple parallel frames (QPF). These allow us to produce films that resemble the Plateau borders of foams and to keep films liquid for up to 120 s [11]. The pulling velocity of 10 mm/s and the melt temperature of 680 °C are kept constant for both model systems.

2.3. Foams

In order to evaluate whether metal films represent the phenomena occurring in foams, corresponding metal foams are produced via gas injection. The gas injection furnace used contains two vertically arranged insulated heating plates, each with 1200 W power, enough to heat up the melt to 680 °C, see Figure 1b). The temperature is recorded by a thermocouple and maintained constant using a power controller. Perpendicular to the heating system, two X-ray transparent boron nitride plates close the furnace. This allow us to study foaming in-situ via a microfocus X-ray source and a flat panel detector [20]. The X-ray spot size on the target is 5 µm.

In the past, mostly static cannulas have been used to inject gas into melts and to convert them into foam. However, such cannulas may be disadvantageous. For example, an overpressure is required to break the oxide skin at the beginning of injection and the oxide filaments blown off might remain in the liquid. Therefore, a moveable cannula system powered by a stepper motor is used that allows one to insert a cannula from the bottom into the melt and to avoid coverage with an oxide film. The gas injection pressure is adjusted by a needle valve and recorded by a sensor. To investigate the influence of the oxygen level of the surrounding atmosphere the furnace is kept inside a gas-tight stainless steel chamber. The oxygen contents of both the injected gas and the atmosphere in the chamber are controlled individually by an "Oxygen Service Controller II" of Prozess-Informatik GmbH, Germany. Before starting the foaming experiments, the chamber is evacuated and purged twice with Ar at a flow rate of 100 l/h. Thereby moisture is removed and the same low oxygen content as for the model system ($\ll$1 ppm O_2) achieved. All experiments are performed at 680 °C at 200–300 mbar gas injection over-pressure and using a conical injection cannula [21]. Varied composites, different oxygen contents and injected gases are applied. Foam expansion as well as the coalescence of bubbles are recorded by the software "HiPic 7.1" and analysed with the software "ImageJ" [22].

2.4. Microstructural analysis

For a microstructural analysis of the particle arrangement at the solid-gas interface of films and foams, a Zeiss CrossBeam 1540 EsB© workstation is used. It comprises a scanning electron microscope (SEM) with an ultra-high-resolution GEMINI© field emission column and two secondary electron detectors, namely an in-lens detector perpendicular to the surface and a lateral assembly SE2 detector (both detect secondary electrons). Moreover, it contains a focused ion beam (FIB) unit, which is used to cut fine lamellae out of the sample surface for the characterisation of the oxide layer by transmission electron microscopy (TEM). The SE2 detector is used for investigating the surface topology, the in-lens detector to observe the milling process and for higher Z-contrast imaging. A 1-µm thick carbon layer is deposited on the surface to protect the oxide layer during milling. Milling is performed with a 30 keV gallium ion beam with a current decreasing in steps from 10 nA and 2 nA to 200 pA to prepare a 10-µm long lamella and to reduce its thickness to <1 µm. After this, the lamella is bonded to a copper grid to further reduce its thickness to <100 nm employing a current of 50 pA and 20 pA. Eventually, the lamella becomes electron transparent, which allows for

investigating the oxide layer using energy-filtered TEM (EFTEM) in a Zeiss LIBRA 200 microscope. The TEM operates at 200 kV and is equipped with a field emission gun and a high-resolution in-column energy filter. In the electron energy loss spectroscopy (EELS) mode this system yields an energy resolution of <0.7 eV. To visualise the oxides at the solid-gas interface, two images are acquired at 510 and 530 eV, which is below the oxygen peak edge at 542 eV. From this image another one taken at 552 eV is subtracted using the imaging software "DigitalMicrograph" [23]. To achieve a high-contrast oxygen map, 15 images with each 10 s exposure time are summed up. For a better evaluation, a further bright-field image of the same area is recorded and overlaid with the intense oxygen image using the software "ImageJ".

2.5. Synchrotron radioscopy and tomography

In-situ visualisation of particles in liquid films is carried out by hard X-ray radioscopy using high-brilliance synchrotron radiation at beamline ID 19 of the European Synchrotron Radiation Facility (ESRF) in Grenoble, France [24]. Imaging with polychromatic radiation is performed in the phase contrast mode with a sample-detector-distance of 1 m and an mean X-ray energy of around 19 keV, thus allowing for the separation of materials of similar electron density, in our case the aluminium alloy and the ceramic particles. The X-ray beam is converted to visible light using a LuAG:Ce single crystal scintillating screen (Ce-doped $Lu_3Al_5O_{12}$). The image is projected onto a "pco.dimax S" CMOS camera through a folded optical system to avoid any damage of the detector. The camera has 2.7 µm pixel size and can cope with frame rates up to 12 fps at full resolution [25]. For our purpose, the gap of the U17.6 single-harmonic undulator is set to 14.5 mm. The field of view is covered by 2016 × 2015 pixels. Images are acquired at 50 fps and 10 ms exposure time, which is found sufficient to track particles in the liquid film. Image processing and visualisation of particles is performed using the software "Image J".

High-resolution tomographies of the solidified films and foams are obtained by taking 2000 images distributed over an angle of 180° in steps of 0.09°. These projections are reconstructed to a 3D model using the software "Octopus 8.6" and analysed using the image processing software "VGStudioMax2.2".

3. Results

3.1. Oxide layers on single films

As it is known from a former study that oxygen is required to stabilise a liquid aluminium alloy film [8], the nature of oxidation is analysed by electron microscopy to obtain more information on the conditions at the solid-gas interface. The films studied are drawn with a single wire frame of 12 mm diameter at 10 mm/s velocity and solidified within 10 s. Starting with SEM, the SiC particles contained in an AlSi9Mg0.6/SiC/20p film are seen to be largely exposed and uncovered at the surface whenever the oxygen level is kept to 200 ppm, see Figure 2a). In contrast, particles in films processed in air (21 % O_2) are totally covered by an oxide layer, see Figure 2b). If such particles are cut to fine lamellae and imaged by TEM, this feature becomes even more evident in cross sections, see Figure 2c) and d). Previously oxidised areas, see wrinkled areas in Figure 3, are arranged in bands that have been pulled apart during extraction of the film from the melt and are separated by freshly oxidised smooth areas.

By applying EFTEM, further structural properties of the oxide layer are revealed. Oxygen-selective images of Al/TiB_2/6p films and remnants of (already ruptured) AlSi9/TiB_2/6p films drawn in air exhibit a discontinuous oxide layer (called ‘oxide islands’ in the following), see red spots in Figure 4a) and b). These characteristic structures are up to 20 nm thick. If Mg is added to the alloy as for AlSi9Mg0.6/TiB_2/6p, see Figure 4c), oxides form a continuous layer of 20–35 nm thickness. A replacement of the particle type (SiC for TiB_2) does not change the properties of the oxide layer, compare Figure 4c) with d). However, if the oxygen content of the atmosphere is reduced to 1000 ppm, a discontinuous broken oxide layer of up to 35 nm thickness is observed, see Figure 4e). Although the oxide thicknesses are quite close together, only films containing Mg and pulled in an atmosphere containing a sufficiently high concentration of oxygen form a continuous layer of oxides of constant thickness. The labels I, II and III express the degree of film stability in Figure 4.

3.2. The behaviour of particles in liquid films

The powerful X-ray beams available at the ESRF and the possibility to work in the phase contrast mode allow us to visualise and analyse particle trajectories in liquid films (drawn using the QPF model system) and even the wrinkled oxide skin of Figure 3a), see Figure 3b). One important observation is that some of the individual particles or particle

clusters either flow continuously (type 1) or are fixed from the very beginning (type 2). Other particles stop their movement at a certain instant and do not move any further (type 3). The latter, at first sight surprising behaviour is studied in more detail for AlSi9Mg0.6/SiC/20p films pulled at an oxygen level of both 1000 ppm and 21 % (air) as well as for AlSi9/TiB_2/6p films pulled in air to elucidate the influence of Mg, of the type of stabilising particles and of the oxygen content. To visualise this effect in maximum clarity, several image processing steps are performed: a first background correction, dilatation of all pixels above a given minimum intensity threshold to emphasise the particles (they become more rounded and slightly larger) and the averaging over groups of 10 frames to blur moving particles. This is followed by the subtraction of a reference image blurred by a Gaussian to equalise brightness variations and finally by subtraction of the average of the first 50 frames to eliminate most of the particles that remain fixed throughout the experiment and highlight particles which are first moving and then become fixed. One example is shown in Figure 5. SiC particles or clusters thereof in an AlSi9Mg0.6/SiC/20p film pulled in air flow downwards under the influence of gravity. The corresponding particle trajectories appear as blurry and dark vertical stripes as we integrate images over 0.2 s, see Figure 5b). Whenever the movement of a particle ends, it appears as a clear structure such as the one marked by a solid black circle in Figure 5c). Another observation is that this immobile cluster in the circle can catch further particles or clusters, see dotted black circle) in Figure 5d) which then also becomes immobile. Supplementary Movie 1 shows the particle flow and attachment in real time.

To quantify the immobilisation of particles and clusters, the coverage of the field of view (FOV) by particles or clusters of a minimum size (each ≥1000 µm²) that are either always moving (type 1) or are first moving and then become immobile (type 3) is determined as a function of time after Figure 5b−d) have been binarised. (Permanently fixed particles of type 2, see Figure 5a), have been largely eliminated from the images by subtracting a reference image). Figure 6 indicates a preferred immobilisation within the first seconds after the film has been pulled out of the melt, during which ~7 % of the FOV of AlSi9Mg0.6/SiC/20p processed in air are filled by immobilised particles. The experiment is carried out twice with similar results. In contrast to this experiment, a film of the same alloy pulled in an atmosphere containing just 1500 ppm oxygen and an AlSi9/TiB_2/6p film pulled in air exhibit a particle coverage of just ~1 % of the FOV and also reach a fairly constant value after a few seconds.

The number of clusters that become fixed (type 3) is related to the number of all clusters mobile in the beginning (type 1+3) in order to avoid a possible misinterpretation based on the total number of particles, which can vary between the individual experiments. These results are summarised in Table 1 and convey information comparable to Figure 6. More than twice as many clusters (than all the moving clusters) become fixed clusters in the AlSi9Mg0.6/SiC/20p film pulled at 21 % O_2 than in the film pulled under 1500 ppm O_2 or in the AlSi9/TiB_2/6p film pulled in air. It is obviously the combination of an enhanced oxygen concentration and the presence of Mg that gives rise to particle immobilisation.

Even though particles of type 2 are not included in the quantitative fixation analysis presented above they are present and together with the particles trapped by them constitute barriers in a film that markedly influence particle flow. In Figure 7 the movement of particles is visualised by colour-coded trajectories, where colours stand for time. Clusters of fixed particles are clearly seen and delimited by white broken lines from the dark background of the particle-free liquid metal. Particles flow freely through the liquid between the clusters and also into the particle clusters (region 1) but few particle trajectories emerge from particle clusters (see regions 2−4), indicating the absence of detachment of particles from existing particles. The conditions can be seen best in the moving image sequence (Movie 2) from which Figure 7 is derived. Particles flow into the fixed clusters. Only for the small fixed clusters most moving particles pass in front or behind those clusters with respect to the viewing direction, whereas the particles get stuck in the larger fixed clusters and cannot pass them. Some particles are seen to be caught by the fixed clusters if this happens at its edge, for example after 2.2 s and 2.8 s by the large particle complex on the lower right.

3.3. The influence of oxygen on foaming particle-containing melts

Knowing now the influence of oxygen on the stability of single films, foams of the same material are produced by selecting different levels of oxygen in the gas injected into the melt as well as in the surrounding atmosphere.

By injecting air and keeping the melt in air too, composites containing solid particles (at least 10 vol.% SiC in AlSi9Mg0.6 or 6 vol.% TiB_2 in AlSi9Mg0.6) can be foamed and expanded continuously, c.f. Figure 8a). Not a single bubble rupture is observed within 30 min of holding after the gas injection has been stopped at t_0, indicating very good stabilisation. In

contrast, alloys with less than the given minimal particle content or composites without Mg (not shown in Figure 8) are not stable and no longer considered.

The oxygen content of the gas injected is reduced to a practical minimum, i.e. ≪1 ppm O_2, whereas the surrounding atmosphere is still air. Injecting such gas leads to less stable foams, i.e. only temporary stability can be achieved and maximum expansion is restricted. Maximum expansion, which leads to foams with an onion-like structure comprising an accumulation of collapsed bubbles on top of the melt, compare Figure 8b), is up to 33.0 mm for AlSi9Mg0.6/TiB_2/6p (from the bottom of the lowest bubble to the top of highest), 33.5 mm for AlSi9Mg0.6/SiC/10p and 42.5 mm for AlSi9Mg0.6/SiC/20p.

By comparing the development of two foams reinforced with 10 % and 20 % SiC during holding after Ar injection has been stopped, a further quantitative factor of particle stabilisation can be identified: bubbles rupture occurs preferably shortly after gas injection has been stopped as seen by the decreasing number of bubbles in Figure 9. The number of ruptures is counted manually. The initial number of foam bubbles is approximated by calculating the projected foam area (different for the two foams) multiplied by its thickness (2 cm, the depth of the furnace) and dividing it through a typical mean bubble volume of the gas injection process (0.11 cm^3 for Ø = 0.6 cm as measured by the line intersection method for both SiC contents). The composite richer in particles gives rise to more stable foams, reflected by the lower number of ruptures detected (15 or 25 ruptures in 600 s for AlSi9Mg0.6/SiC/20p or AlSi9Mg0.6/SiC/10p, respectively). AlSi9Mg0.6/TiB_2/6p cannot be quantified because only bubbles at the very top of the foam are stable. All following bubbles reaching the foam on top of the melt collapse immediately.

In a further experiment, the oxygen content of the surrounding atmosphere is also reduced to ≪1 ppm. Under such circumstances, only few bubbles generated in AlSi9Mg0.6/SiC/10p are temporally stable (but eventually merge with other bubbles), whereas most of the bubbles rupture immediately after reaching the surface of the melt. This aspect of foam destabilisation by excluding oxygen from both the injection gas and the surrounding atmosphere is illustrated in Figure 8c). For AlSi9Mg0.6/SiC/20p and AlSi9Mg0.6/TiB_2/6p with their higher particle contents, this destabilisation effect is less pronounced. These composite foams reach maximum expansions of 33 mm for AlSi9Mg0.6/SiC/20p and 32.5 mm for AlSi9Mg0.6/TiB_2/6p even in the very pure argon environment (foams not shown).

In one experiment, an argon-filled hemisphere (a big bubble resting on top of a AlSi9Mg0.6/SiC/20p melt) is generated in an accidental event, see Figure 10. In this hemisphere, the freshly created melt surface – the straight part of the line in Figure 10a) – is exposed to oxygen to the smallest possible extent. In contrast to this very pure atmosphere and surface, the melt surfaces of earlier experiments are likely contaminated by some small amounts of oxides during preparation and melting, allowing for foam structures as shown in Figure 8b-c) that are characterised by an onion-like structure of collapsed cells on the top, see discussion section. Now, if injected Ar bubbles reach the melt surface of the Ar hemisphere from below they rupture immediately, see Figure 10b) and c), even for the highest achievable particle concentration of 20 vol.% SiC. Supplmentary Movie 3 shows these phenomena in real time.

To answer the question why oxygen improves foam stability so tremendously, some microscopic investigations are carried out on solidified foams, see Figure 11. Accordingly, the SiC particles in AlSi9Mg0.6/SiC/20p are distributed over the entire Plateau border cross section if air is used for gas injection, Figure 11a), whereas for Ar injection almost no particles can be detected in the centres of the Plateau borders, Figure 11b). The sample for the Ar-blown foam is extracted from a semistable foam such as the one shown in Figure 8b). X-ray tomographies of further samples confirm this observation in a three-dimensional volume as well, Figure 11c,d). SEM on the solid-gas interface of a bubble reveals that particles are embedded deeper into the surface and covered by an oxide layer if air is used for foaming, Figure 11e). In contrast, particles in foams blown by Ar gas are loosely connected to the surface and largely exposed, Figure 11f). EFTEM shows that air-foamed samples exhibit an oxide layer of constant thickness of 30–50 nm at the inner bubble surface, Figure 11g), while the less stable argon-blown foams exhibit an irregular oxide layer. Areas up to 50 nm (oxide islands) are visible, but are interrupted by thin uncovered areas of just 10–20 nm thickness, Figure 11h).

4. Discussion

4.1. Stabilisation by particles

It is known that solid particles such as SiC or Al_2O_3, in metal foams created by gas injection influence stability [26], see also Figure 9, or are even mandatory [12, 14]. In our

case, the trend is similar: only AlSi9Mg0.6 containing more than 10 vol.% SiC or 6 vol.% TiB_2 can be foamed, compare to chapter 3.3.

In earlier work, even single films of Al not containing particles have been found to be temporarily stable provided that drainage is kept low by drawing the wire frame out of the melt quickly, thus interrupting contact with the melt and leading to solidification within 10 s [8]. In contrast, when the films are kept liquid they eventually rupture, similar to what happens to some foams [11]. Only films containing Mg and solid particles can be stabilised for up to 30 s (AlSi9Mg0.6/SiC/20p) or for even longer than 120 s (AlSi9Mg0.6/TiB_2/6p).

One interaction of Mg with the particles in the liquid state is revealed by in-situ synchrotron radioscopy on liquid films: more than twice as many SiC particles are captured and immobilised if the alloy contains Mg, see Figure 5, Figure 6 and Table 1. An idea of how Mg interacts with particles has been presented by Asavavisitchai et al. [2]: They report that Mg improves wetting of SiC by the melt. As a consequence, particles are dragged deeper into the metallic film, thus hindering drainage more effectively. The reason for the good wettability is in turn addressed by Pai et al., who attribute this effect to spinel particles formed in the surficial SiO_2 layer on SiC particles [27]. Similar effects could act on TiB_2 particles too.

Some authors relate foam stabilisation to the distribution of particles in liquid foams. Three ideas have been brought up in the literature: (i) Kaptay claims that particles form bridges between opposite liquid/gas interfaces and prevent them to come closer to each other due to mechanical forces [28]. (ii) Kumagai et al. suggest that particles change the cell wall curvature and reduce capillary suction into Plateau borders [29]. (iii) Blockage of thin sections of the foam by agglomerations of particles that form barriers and the associated retarded flow of liquid out of the foam has also been proposed [30, 31]. Experimental evidence for any of these mechanisms is partially missing or sometimes even contradictory. Most likely more than one mechanism applies and the circumstances depend on the type of foam studied.

Kaptay's bridge model (i) has been ruled out for foams containing SiC particles and blown with hydrogen since the particles strongly segregate to the gas/metal interfaces and the space in between contained to few particles to allow for the formation of bridges [5]. However, in the present work, the density of particles in the Plateau borders and in the films of the foams blown with air appears so high that the bridge model seems possible, see Figure 11a) and c). An influence of film curvature (mechanism ii) has been found experimentally for

liquid Al films [11]. The barrier mechanism (iii) can be found in liquid films pulled in air, see Figure 7. Moving particles (type 1+3, coloured trajectories) can attach to already fixed clusters (type 2 or 3, white spots delimited by a white broken line) that increasingly act as a barrier for flowing particles. Such barriers extend from one liquid-gas interface to the other as one can deduce from the observation that no particles that are flowing behind or in front of the barriers can be detected. The only visible flow is that into clusters and terminating there or through the tortuous system of residual open melt channels (dark areas in Fig. 7). These barriers could transmit forces – Kaptay's model (i) – or reduce melt flow – barrier model (iii) –, or both, but which mechanism is acting cannot be deduced from the images.

4.2. Stabilisation by oxygen

Oxygen is already known to improve foam stability [12] or even to be required to build single Al films [8]. In Figure 8, the beneficial action of oxygen for foaming can be clearly seen. If oxygen is excluded from both the injection gas and the surrounding atmosphere foam formation is minimal. The presence of oxygen in the surrounding atmosphere is sufficient to create some (however not much) foam stability via oxidation of the outer surface of the foam, even though Ar is used to create the bubbles. This underlines the efficiency of oxygen to stabilise metal foams.

The analysis of films by oxygen-sensitive EFTEM analysis shows how oxygen acts: if no Mg is present only a partially stable film of Al/TiB_2/6p can be drawn in air [8], which then exhibits a partial and interrupted oxide coverage only, the oxide islands in Figure 4a). For AlSi9/TiB_2/6p, no film can be drawn [8], while the oxide islands look similar, see Figure 4b). In contrast, for AlSi9Mg0.6 both particle-containing films (SiC and TiB_2) are stable [8] and exhibit a similar oxide layer of constant thickness, see Figure 4c-d). Foams of the same composition follow this trend with only foams containing Mg being stable, compare chapter 3.3 and Figure 11g). The reason why Mg plays such an important role for film and foam stabilisation is connected to the accelerated oxidation kinetics of Al-Mg alloys. Only 1 at.% of Mg accelerates the growth of an oxide film tremendously [32]. Drouzy et al. and DebRoy et al. have found that in the very first stage of oxidation, amorphous MgO is formed next to an Al_2O_3 layer [33, 34]. As only 0.6 wt.% Mg is used and the temperature is 680 °C spinel is the dominant final reaction product [35]. In the course of the reaction, however, transition phases such as Mg-Al-O, Mg-Al-O-Si or Al-Mg-O can occur as well. Furthermore, Mg and oxygen

are known to reduce the surface tension of Al, thus reducing capillary suction into Plateau borders which contributes to foam stability [9]: Goumiri et al. find that the surface tension of Al at 700 °C drops from 1050 mN/m (unoxidised) to 865 mN/m (oxidised) [36]. By the addition of just 1 wt.% Mg the surface tension drops again down to just 650 mN/m [27]. After adding 8 wt. % Si (AlSi8Mg1) this drop is partially reversed to 830 mN/m at 700°C [37].

To study the effect of oxygen in more depth, the oxygen concentration is successively reduced in film pulling experiments. One observes that films become more instable and rupture if a critical oxygen concentration falls below a typical limit, e.g. 200 ppm O_2 for AlSi9Mg0.6/SiC/20p [8]. If a film of that Mg-containing composite is drawn in an atmosphere with an oxygen concentration above its critical concentration, e.g. 1000 ppm O_2, a similar oxidation behaviour as for the composite without Mg but pulled in air can be found, compare Figure 4a-b) and e), even though the film is still stable. Obviously, Mg as well as a minimum amount of oxygen both promote the formation of an oxide layer independently, but only in the presence of both the layer is dense and not interrupted. Furthermore, Jeurgens et al. report a similar morphology of oxide islands at 400 °C and 2×10^4 s holding time for pure Al similar to the ones of Figure 4a), b) and e) [38]. As Thiele and Nylund et al. have shown that the growth of an oxide skin is accelerated by an increased temperature or longer holding time [32, 39] the findings of Jeurgens et al. should be also valid at the higher temperatures applied here. Therefore, the oxide islands of Figure 4a), b) and e) appear as a preliminary stage of the strong continuous oxide layer of Figure 4c) and d).

For foams, a similar trend is found: if foams are made by Ar injection but surrounded by air only partially stable foams can be produced. Foams are fully stable only if the bubble-forming gas also contains oxygen, see Figure 8a) and b). The morphology of the oxide skins also shows similar trends for films and foams: Foams made by Ar injection exhibit a varying oxide layer thickness in contrast to foams made by injecting air, see Figure 11g) and h). Hence, the continuous oxide layer on the outer side of the foam in contact with air is the reason for the onion-like structure in Figure 8b). These oxide films stiffen the outer bubble surfaces and prevent them from disappearing after rupture, while being insufficient to stabilise the bubble against rupture. If the melt is surrounded by an Ar atmosphere, not even an onion-like structure is obtained and most of the bubbles rupture, see Figure 8c) without the oxide remnants of the former bubble surfaces piling up.

As all of these suggested stabilisation mechanisms cannot be assigned to particles (see previous section) or oxygen alone, a more complex model explaining the interactions between particles and oxidation is required.

A direct experimental proof that foams cannot be stabilised without the presence of oxides is achieved by analysing the phenomena inside a hemisphere filled with argon gas, see Figure 10. A freshly formed melt surface exposed to oxidation only for the shortest possible time span is observed. Bubbles ascending from below are instable even if the melt contains 20 vol.% SiC. Unlike in Figure 8c), where some residual foam stability is observed, there are no stable films in this case. It requires the elimination of residual traces of oxygen to show that foams are instable even if the melt contains a high volume fraction of particles.

4.3. A stabilisation model based on particles and oxygen

Scanning electron microscopy reveals pronounced interactions between particles and oxygen for both films and foams, see Figure 2 and Figure 11e) and f). Particles are embedded deeper below the surface and are covered by a thick oxide skin, compare Figure 3, if the oxygen concentration in the atmosphere surrounding the melt is high. Such coverage has been observed before in similar systems [12, 13].

As displayed in Figure 5, moving particles in a liquid film sometimes suddenly stop. Most of this fixation occurs shortly after the film has been drawn, see Figure 6. Furthermore, this phenomenon appears preferentially if the film is drawn in air and the alloy contains Mg, in which case more than twice as many of particles become fixed, compare Table 1 and Figure 6. At this point, the connection of particles and oxygen becomes conspicuous by the analogy between a time-dependent fixation of particles (Figure 6) to an also time-dependent oxidation if more oxygen or Mg are present (chapter 4.2). The EFTEM images in Figure 4 and Figure 11 suggest that a sufficiently thickly grown and continuous oxide skin such as the one shown in Figure 3 is the prerequisite for keeping particles at a fixed position. Hence, the oxide skin can be seen as an immobilising, rigidifying analogue to surfactants in aqueous foams: they both fix particles, retard drainage and stabilise foams [40, 41]. Although the oxide skin is described to be rigid, it is found to rupture and start forming a fresh oxide skin immediately, see Figure 3, which gives the bubble surface a degree of elasticity that allows it to grow, move and expand.

The barrier mechanism displayed in Figure 7 approves this model as well. If the film surfaces were totally liquid (no oxide film), no mechanical forces would act on the particles inside the film which could fix them (except for the weak interparticle forces). Particles would flow with the melt, not be immobilised and merely increase the viscosity of the melt. Previous work supports the necessity of an immobilised oxide skin as well [8]: even for high particle concentrations, i.e. 6 vol.% TiB_2 or 20 vol.% SiC, no stable films can be pulled in an inert gas atmosphere or if the melt does not contain Mg and no oxide skin is created [11].

In Figure 8, a similar trend as for films can be found for foams: If Ar is injected, foams cannot be foamed continuously. Largely uncovered particles are situated on top of the surface (compare Figure 11e) and f), films: Figure 2) and the oxide layer varies in thickness and is in parts thin in contrast to when air is injected (compare Figure 11g) and h), films: Figure 4). The reason why so few particles can be found in the centre of foams blown with Ar, see Figure 11b) and d), is related to the process of the generation of a film or foam, which is depicted schematically in Figure 12. This depiction is based on experimental evidence derived from films for the first 120 s and from foams after.

In both cases (film or foam), a new liquid-gas interface is created in a first step at '0 s'. What happens within the very first seconds (<5 s) with respect to oxidation cannot be observed directly. Directly after the film has been drawn the freshly formed surface is thought to exhibit a direct transition from the liquid to the gaseous phase without much oxide skin (black line). Only some particles adhere to the liquid-gas interfaces as images taken after solidification show, see Figure 2 and Figure 11e) and f). In the liquid state, such particles are thought to freely float on the surface (yellow circles), possibly interacting with each other and increasing surface viscosity, whereas the remaining particles located more towards the centre of films or Plateau borders (red circles) flow unhindered as long as the film channel is much wider than the diameter of particle clusters. The fact that many particles become fixed within the very first seconds, see Figure 6, suggests that partially wetted particles situated at a liquid-gas interface are overgrown by the developing oxide layer and therefore become pinned at their present locations. This will happen more frequently and perhaps more quickly if oxidation is fast due to the presence of much oxygen and Mg. The time until the oxide layer is created is too short to allow for more particles to attach to the interfaces although this might be energetically favourable. After the oxide layer has grown no further segregation of particles to the liquid-gas interface can take place since the gas phase is now inaccessible.

In the following, oxidation creates a growing surface oxide layer, either interrupted thin layers in an oxygen-reduced atmosphere (green in Figure 12) or dense layers of constant thickness in air (blue). Synchrotron radioscopy shows that particles are increasingly immobilised with time as they form clusters (circles with grey filling), compare Figure 5 and Figure 6. Only a continuous oxide skin formed in the presence of oxygen and Mg is strong enough to catch and fix more particles, see also Table 1. Furthermore, only particles attached to that strong oxide skin appear to be fixed strongly enough to catch other particles and keep them at a fixed position (0–120 s), see Figure 5. If argon is injected this mechanism is not active and most of the particles leave the Plateau borders over the time (600 s), after which only few particles can be found in the centre of the Plateau borders, compare Figure 11a), b), c) and d).

4.4. Other types of foam

Aluminium-based foams can be created from consolidated powder mixtures ('PM foams'). These contain a network of fine oxide filaments stemming from the former powder particle surfaces [42] rather than defined particles and the foam stabilisation mechanism differs too much from that of the present foams to be directly compared [43]. Foams created by gas release using a blowing agent in the melt (Formgrip or Alporas process [44, 45]) are more similar, especially when Al alloys with dispersed SiC particles are used as for Formgrip. In fact, Formgrip foams are similar in structure to the foams blown with Ar of this paper, see Figure 11b), as the SiC particles predominantly segregate to the gas/metal interfaces and no particle bridges are observed [5]. The reason is that the blowing gas is hydrogen and oxidation is therefore limited. However, Formgrip foams are more stable than the Ar-blown foams of this paper, see Figure 8b). Various reasons for this can be given. Formgrip precursors contain many small gas-filled pores prior to foaming and might be partially oxidised due to the stirring step of the melt during their manufacture. Moreover, the bubble generation process for Formgrip is totally different: many small bubbles grow simultaneously and are stationary as opposed to the injection of individual bubbles that drift through the liquid in this paper. Finally, the bubbles in Formgrip are notably smaller. Altogether this might facilitate bubble stability in Formgrip foam [44].

4.5. Estimation of drainage rate

To further elucidate the question of foam stability, two drainage models for liquid films available in the literature are discussed. The first approach takes into account the Navier-Stokes equation, and describes the so-called *plug flow* of a liquid film without a solid surface under the influence of gravity [46]. We define a vertical square plate of width *l*, height *h* and thickness *x*, with the corresponding film area *A* and volume *V* as shown in Figure 13. This model describes thinning as a continuous loss of liquid by the flow out of the volume, where viscosity is the only force counteracting drainage. The corresponding film thickness evolution is given by [46]:

$$x_{\mathrm{plug}}(t) = x_0 e^{\left(-\frac{\rho g h}{2\mu} t\right)}, \tag{1}$$

With g the acceleration of gravity, ρ the melt density and μ melt viscosity (3.3 mPas, approximated for AlSi6,5/SiC/20p at 700 °C [47]). Figure 13 shows the film thickness evolution for an AlSi9Mg0.6/SiC/20p film with $l = h = 10$ mm and $x_0 = 4$ mm for a viscosity enhanced by a factor of 10^4. Despite this unrealistically high viscosity value the liquid film loses almost all liquid within few seconds.

The second approach [46] is based on Hagen-Poiseuille flow of a viscous fluid and is based on calculations of Brady et al. [48] where other than in the first approach, the film surfaces are considered rigid, as it would be the case for an immobilising oxide skin. The loss of film volume $V = lhx$ is given then by [46]:

$$-\frac{dV(t)}{dt} = \frac{l\rho g x^3}{12\mu}. \tag{2}$$

Integration of Eq. (2) and regrouping leads to

$$x_{\mathrm{HP}}(t) = x_0 \sqrt{\frac{6\mu h}{\rho g t x_0^2 + 6\mu h}} \tag{3}$$

The corresponding film thickness evolution is also given in Figure 13.

By comparing these results with experimental thickness values of stable solid films (red region based on individual measurements and values reported in the literature [12, 26]) it can be seen that all models thin the film too fast and the critical film thickness ~50 µm for the given system is already reached within seconds, although real films can remain stable for

longer holding times. Comparing *plug* and Hagen-Poiseuille flow, however, shows that a rigid skin can be considered a prerequisite to stabilise a film. *Plug flow* will lead to extreme film thinning and unhindered film rupture even if unrealistically high viscosity values (here $\times 10^4$) are used.

Experiments show that particles drain fast at the beginning but decelerate within the first seconds (Figure 7) and a constant end thickness is approached asymptotically, whereupon the film remains stable. The trend given by Hagen-Poiseuille flow appears plausible if one takes into account that solid barriers in the liquid (Figure 7) or fixed particles (Figure 5) further retard drainage and delay thinning.

A more complete modelling of drainage has to include capillary forces too and can be used to determine the viscosity of melt the foam [49, 50]. Such approaches yield viscosity values much higher than the ones assumed above, thus indicating that there are other factors delaying drainage. A detailed analysis of such effects is beyond the scope of the present paper.

5. Conclusions

- Aluminium melt containing ceramic particles is processed to individual films and to foams, the former by pulling wire frames, the latter by injecting gas into the melt directly. Individual liquid metal films are found to represent metal foams very well as they are stabilised in a similar way.
- The presence of Mg in an alloy as well as an oxidising environment during film pulling or foaming are both prerequisites for the stability of liquid films and foams. Gas-liquid interfaces are covered by an immobilising oxide skin due to oxidation.
- These oxide skins on films or foams cover the stabilising particles and push them to below the melt surface. This is required to prevent them from flowing out of the film and rather to be immobilised by interactions with other particles, thus building up barriers to further flow.
- The oxide skins are not thick enough to impede film expansion. The skins can be stretched and even rupture, but are formed again immediately after.
- An increased melt viscosity due to the presence of particles is not sufficient for stabilisation.

- It is found that also oxygen and not only particles are necessary for stabilisation. Even at the highest particle concentration considered (20 vol.% SiC) foams are not stable if there is no oxygen in the environment. The stabilisation of films and foams is therefore based on the interaction of oxygen and particles.

Acknowledgements

The author thanks M. Wollgarten for his introduction into EFTEM. This study was supported by the German DFG, grants GA 1304/2-1 and BA 1170/17-1.

References

[1] Wübben T, Odenbach S. Stabilisation of liquid metallic foams by solid particles. Colloids and Surfaces A: Physicochemical and Engineering Aspects 2005;266:207.

[2] Asavavisithchai S, Kennedy AR. The effect of Mg addition on the stability of Al–Al2O3 foams made by a powder metallurgy route. Scripta Materialia 2006;54:1331.

[3] Banhart J. Metal foams: Production and stability. Advanced Engineering Materials 2006;8:781.

[4] Liu X, Li Y, Chen X, Liu Y, Fan X. Foam stability in gas injection foaming process. Journal of Materials Science 2010;45:6481.

[5] Haibel A, Rack A, Banhart J. Why are metal foams stable? Applied Physics Letters 2006;89:1541021.

[6] Babcsán N, Leitlmeier D, Degischer HP. Foamability of particle reinforced aluminum melt. Materialwissenschaft und Werkstofftechnik 2003;34:22.

[7] Vinod Kumar GS, Garcia-Moreno F, Babcsán N, Brothers AH, Murty BS, Banhart J. Study on aluminium-based single films. Physical Chemistry Chemical Physics 2007;9:6415.

[8] Heim K, Vinod Kumar GS, Garcia-Moreno F, Banhart J. Role of Ambient Oxygen in the Stabilisation of Single Aluminium Alloy Films. Procedia Materials Science 2014;4:251.

[9] Pugh RJ. Foaming, foam films, antifoaming and defoaming. Advances in Colloid and Interface Science 1996;64:67.

[10] Wasan DT, Nikolov AD, Lobo LA, Koczo K, Edwards DA. Foams, thin films and surface rheological properties. Progress in Surface Science. 1992;39:119.

[11] Heim K, Vinod Kumar GS, Garcia-Moreno F, Manke I, Banhart J. Drainage of particle-stabilised aluminium composites through single films and Plateau borders Colloids and Surfaces A Physicochemical and Engineering Aspects 2013;438:85.

[12] Leitlmeier D, Degischer HP, Flankl HJ. Development of a foaming process for particulate reinforced aluminium melts. Advanced Engineering Materials 2002;4:735.

[13] Babcsán N, Leitlmeier D, Degischer HP, Banhart J. The role of oxidation in blowing particle-stabilised aluminium foams. Advanced Engineering Materials 2004;6:421.

[14] Ip SW, Wang Y, Toguri JM. Aluminum foam stabilization by solid particles. Canadian Metallurgical Quarterly 1999;38:81.

[15] Kaptay G. Interfacial criteria for stabilization of liquid foams by solid particles. Colloids and Surfaces A: Physicochemical and Engineering Aspects 2003;230:67.

[16] Babcsán N, Garcia-Moreno F, Banhart J. Metal foams - High temperature colloids: Part II: In situ analysis of metal foams. Colloids and Surfaces A: Physicochemical and Engineering Aspects 2007;309:254.

[17] Garcia-Moreno F, Solórzano E, Banhart J. Kinetics of coalescence in liquid aluminium foams. Soft Matter 2011;7:9216.

[18] Banhart J, Stanzick H, Helfen L, Baumbach T. Metal foam evolution studied by synchrotron radioscopy. Applied Physics Letters 2001;78:1152.

[19] Vinod Kumar GS, Babcsán N, Murty BS, Banhart J. Verfahren zur Herstellung von Metallschäumen und Metallschaum. German Patent Application DE 10 2006 031213.9, 2007.

[20] García Moreno F, Fromme M, Banhart J. Real-time X-ray radioscopy on metallic foams using a compact micro-focus source. Advanced Engineering Materials 2004;6:416.

[21] García-Moreno F, Siegel B, Heim K, Meagher AJ, Banhart J. Sub-mm sized bubbles injected into metallic melts. Colloids and Surfaces A: Physicochemical and Engineering Aspects in press.

[22] Schneider CA, Rasband WS, Eliceiri KW. NIH Image to ImageJ: 25 years of image analysis. Nature Methods 2012;9:671.

[23] Reimer L, Zepke U, Moesch J, Schulze-Hillert S. EELspectroscopy: a reference handbook of standard data for identification and interpretation of electron energy loss spectra and for generation of electron spectroscopic images. Oberkochen: Carl Zeiss, Electron Optics Division, 1992.

[24] Rack A, Garcia-Moreno F, Schmitt C, Betz O, Cecilia A, Ershov A, Rack T, Banhart J, Zabler S. On the possibilities of hard X-ray imaging with high spatio-temporal resolution using polychromatic synchrotron radiation. Journal of X-Ray Science and Technology 2010;18:429.

[25] Garcia-Moreno F, Rack A, Helfen L, Baumbach T, Zabler S, Babcsán N, Banhart J, Martin T, Ponchut C, Di Michiel M. Fast processes in liquid metal foams investigated by high-speed synchrotron x-ray microradioscopy. Applied Physics Letters 2008;92:1341041.

[26] Wang D, Shi ZY. Effect of ceramic particles on cell size and wall thickness of aluminum foam. Materials Science and Engineering A 2003;361:45.

[27] Pai BC, Ramani G, Pillai RM, Satyanarayana KG. Role of magnesium in cast aluminium alloy matrix composites. Journal of Materials Science 1995;30:1903.

[28] Kaptay G. Interfacial criteria for producing metal matrix composites and ceramic particle stabilized metallic foams. Materials Science Forum 2003;414-415:419.

[29] Kumagai H, Torikata Y, Yoshimura H, Kato M, Yano T. Estimation of the stability of foam containing hydrophobic particles by parameters in capillary model. Agricultural and Biological Chemistry 1991;55:1823.

[30] Banhart J. Manufacturing routes for metallic foams. JOM Journal of the Minerals 2000;52:22.

[31] Wübben T. Zur Stabilität flüssiger Metallschäume: Universität Bremen, 2004.

[32] Thiele W. Die Oxidation von Aluminium- und Aluminiumlegierungsschmelzen. Aluminium 1962;38:707.

[33] DebRoy T, Bandopadhyay A, Roy R. Oxide matrix composite by directional oxidation of a commercial aluminum-magnesium alloy. Journal of the American Ceramic Society 1994;77:1296.

[34] Drouzy M, Mascré C. The oxidation of liquid non-ferrous metals in air or oxygen. Metallurgical Reviews 1969;14:25.

[35] McLeod AD, Gabryel CM. Kinetics of the growth of spinel, MgAl2O4, on alumina particulate in aluminum alloys containing magnesium. Metallurgical Transactions A 1992;23:1279.

[36] Goumiri L, Joud JC. Auger electron spectroscopy study of aluminium-tin liquid system. Acta Metallurgica 1982;30:1397.

[37] Goicoechea J, Garcia-Cordovilla C, Louis E, Pamies A. Surface tension of binary and ternary aluminium alloys of the systems Al-Si-Mg and Al-Zn-Mg. Journal of Materials Science 1992;27:5247.

[38] Jeurgens LPH, Sloof WG, Tichelaar FD, Mittemeijer EJ. Structure and morphology of aluminium-oxide films formed by thermal oxidation of aluminium. Thin Solid Films 2002;418:89.

[39] Nylund A, Mizuno K, Olefjord I. Influence of Mg and Si on the oxidation of aluminum. Oxidation of Metals 1998;50:309.

[40] Koehler SA, Hilgenfeldt S, Weeks ER, Stone HA. Foam drainage on the microscale II. Imaging flow through single Plateau borders. Journal of Colloid and Interface Science 2004;276:439.

[41] Saulnier L, Restagno F, Delacotte J, Langevin D, Rio E. What is the mechanism of soap film entrainment? Langmuir 2011;27:13406.

[42] Dudka A, Garcia-Moreno F, Wanderka N, Banhart J. Structure and distribution of oxides in aluminium foam. Acta Materialia 2008;56:3990.

[43] Körner C, Arnold M, Singer RF. Metal foam stabilization by oxide network particles. Materials Science and Engineering A 2005;396:28.

[44] Gergely V, Clyne B. The FORMGRIP process: foaming of reinforced metals by gas release in precursors. Advanced Engineering Materials 2000;2:175.

[45] Miyoshi T, Itoh M, Akiyama S, Kitahara A. Alporas aluminum foam: Production process, properties, and applications. Advanced Engineering Materials 2000;2:179.

[46] Laimböck P. Foaming of glass melts: Technische Univeriteit Eindhoven, 1998.

[47] Garcia-Moreno F, Tobin ST, Mukherjee M, Jiménez C, Solorzano E, Vinod Kumar GS, Hutzler S, Banhart J. Determination of melt surface tension and viscosity in liquid aluminium alloy foams through microgravity experiments. (in work) 2013.

[48] Brady AP, Ross S. The measurement of foam stability. Journal of the American Chemical Society 1944;66:1348.

[49] Gergely V, Clyne TW. Drainage in standing liquid metal foams: Modelling and experimental observations. Acta Materialia 2004;52:3047.

[50] Garcia-Moreno F, Tobin ST, Mukherjee M, Jimenez C, Solorzano E, Kumar GSV, Hutzler S, Banhart J. Analysis of liquid metal foams through X-ray radioscopy and microgravity experiments. Soft Matter 2014;10:6955.

TABLE

Table 1. Number of particle clusters per mm² of a metal film with an area of each cluster >1000 µm² observed 10 s after film is pulled from a melt of the given composition. Always mobile (type 1) and initially moving clusters that then are immobilised (type 3) are counted. As these are individual experiments, no error is given.

Material	Number of immobilised clusters (type 3)	Number of clusters (type 1+3)	type 3 / (type 1 + 3)
AlSi9/TiB_2/6p, 21 % O_2	1.8	17.6	10.2%
AlSi9Mg0.6/SiC/20p, 21 % O_2	6.2	31.2	19.9%
AlSi9Mg0.6/SiC/20p, 1500 ppm O_2	2.3	24.3	9.5%

FIGURES

Figure 1. a) Schematic cross section of the film pulling set-up featuring the heated crucible and the stirring and film pulling devices. b) Gas injection furnace with moveable injection cannula used for the foaming experiments.

Figure 2. SEM image (taken with the secondary electron (SE2) detector) of SiC particles at the surface of an AlSi9Mg0.6/SiC/20p film drawn in an atmosphere containing a) 200 ppm and b) 21 % oxygen. c,d) corresponding cross sections captured with the in-lens detector during the preparation of TEM samples using a focussed ion beam.

Figure 3. Wrinkled and ruptured oxide skin on the freshly oxidised surface of an AlSi9Mg0.6/SiC/20p film pulled in air. a) SEM image (taken with the secondary electron (SE2) detector) of a sample made using the SF model and solidified immediately after pulling. b) Synchrotron X-ray radiography taken in the liquid state of another sample of the same material. Film made by pulling the QPF model out of a melt at 680 °C.

Figure 4. Overlay of TEM bright-field images with oxygen-sensitive EFTEM images (red spots indicate oxygen in oxides) showing the solid-gas interface of a single film (SF, solidified within 10 s) pulled in an atmosphere containing 21% O_2 (a-d) or at 1000 ppm oxygen partial pressure (e). Various systems are investigated: a) Al/TiB_2/6p, b) AlSi9/TiB_2/6p, c) AlSi9Mg0.6/TiB_2/6p and d,e) AlSi9Mg0.6/SiC/20p. The side of the alloy is the one with the composition label. Roman numerals denote whether a film is stable (I), semistable, i.e. stable for small wire frame diameters only (II) or unstable (III).

Figure 5. Synchrotron X-ray radiographies (E = 19 keV) of an AlSi9Mg0.6/SiC/20p film pulled in air at 680 °C. a) single image of the state immediately after the end of pulling when the liquid film has come to a rest, b) after integrating over the first 0.2 s and image processing, c,d) same as b) but integrated image 1.7 s or 4.1 s after pulling, respectively. e) shows again the final raw radioscopy 10 s after pulling. Dark blurred vertical stripes indicate particles in motion. Sharp, clearly recognisable spots represent individual particles or particle clusters originally in motion but now immobile and at a fixed position (type 3). Solid circle in c) marks such an exemplary immobilised particle, to which in d)

a further cluster attaches (broken circle). The horizontal stripes in a) and e) are caused by fluctuations of the beam and not by the sample. The phenomena discussed in this figure can be seen in real time in supplementary Movie 1.

Figure 6. Analysis of films pulled with the QPF model. Area within the FOV in film covered with particle clusters that are first mobile and then fixed (type 3) and have each more than 1000 µm² area, expressed as a fraction of the total area of the FOV. Three combinations of material and oxygen concentration are investigated. In one case an experiment is duplicated.

Figure 7. SiC particle trajectories (type 1+3) in a AlSi9Mg0.6/SiC/20p film pulled in air from a melt at 680 °C. This visualisation is obtained by image processing, particle tracking and temporal integration over 6 s of a series of synchrotron X-ray radiographies taken at 19 keV energy. The colour scale defines particle positions at a given time (in seconds) shown in the period a) 6–12 s and b) 12–18 s after pulling. White broken lines denote boundaries between free melt and already fixed immobile clusters (type 2 + 3) appearing as white spots. '1' marks a region where particles flow into an already fixed cluster, regions '2−4', where no particles emerge from inside, behind or in front of the clusters. Movie 2 provides an impression how particles move through this structure in real time.

Figure 8. X-ray radioscopies of AlSi9Mg0.6/SiC/10p foam blown by injecting a) air or b) argon. Both foams are surrounded by air. c) Argon is injected and foam is surrounded by Ar atmosphere. The images are taken after stopping bubbling and holding at 680 °C for 600 s.

Figure 9. Number of bubbles left after holding for a given time at 680 °C after foams have been created by bubbling argon into AlSi9Mg0.6/SiC/10p or AlSi9Mg0.6/SiC/20p melts for 15 s. The melt is surrounded by air.

Figure 10. X-Ray radioscopy of ascending bubbles that reach the surface and rupture immediately. The point of interest lies within a large argon filled semisphere produced by a rising argon bubble previously (broken line on left). The arrows show where successive smaller argon bubbles ascend and rupture at the interface to the larger argon-filled volume. Images are recorded every 250 ms. The AlSi9Mg0.6/SiC/20p melt is kept at 680 °C for the experiment. The process of bubble rupture can be followed in real time in supplementary Movie 3.

Figure 11. Metallographic cross sections of Plateau borders in AlSi9Mg0.6/SiC/20p foams produced by injecting a) air or b) Ar gas. Synchrotron X-ray tomography of the same foams: c) green spots indicate SiC and their distribution inside a Plateau border; d) red spots indicate SiC particles and their tendency to remain at the solid-gas interface. e,f) SEM images of SiC particles at the inner bubble surface. g,h) overlay of a TEM bright-field image with an oxygen sensitive EFTEM image at the solid-gas interface of the same foam (red spots mark the oxides). 'Matrix' indicates the side of the alloy.

Figure 12. Schematic model of the processes and particle movements in single metallic films and films in foams depending on the oxygen concentration in the environment of the film or in the gas used to blow the foam. Red circles indicate fast flowing particles in the centre of the film, yellow circles are slowly flowing and barely wetted particles at the liquid-gas interfaces, while solid black dots are particles that have been immobile from the very beginning (type 2). Grey circles represent immobilised clusters that have been initially mobile (type 3) or are static due to solidification. The black margins of the film surface (0 s) indicate a direct transition of the liquid to the gaseous phase. The following blue margins mark a continuous oxide skin, in contrast to a surface structure consisting of oxide islands (green margins).

Figure 13. Comparison of the thickness reduction with time of an AlSi9Mg0.6/SiC/20p film governed either by gravity-driven plug flow (viscosity increased $\times 10^4$) or Hagen-Poiseuille flow (yellow area indicating the immobilising oxide skins) or by capillary-driven flow. The red bar indicates the experimentally determined critical film thickness range in liquid foams.

Supplementary Material

Movie 1. Synchrotron X-ray radioscopy showing SiC particles flowing through a AlSi9Mg0.6/SiC/20p film pulled in air at 680 °C. Images of Figure 5 are taken from this movie. Left: background corrected raw data, centre: images after integration over 0.2 s and image processing. right: images after binarisation as used for the quantitative analysis (see Figure 6). Movie is recorded immediately after the end of pulling and shows the processes in real time. Dark blurred vertical stripes indicate particles in motion. Sharp, clearly recognisable spots represent individual particles or particle clusters originally in motion but now immobile and at a fixed position.

Movie 2. SiC particles flowing through a AlSi9Mg0.6/SiC/20p film pulled in air from a melt held at 680 °C. Each frame of the movie is an average over 0.2 s and the image sequence represents a floating average, which is why the particles appear as short dashes. Real time is given on bottom right. Figure 7 is derived from this image sequence.

Movie 3. X-Ray radioscopy of rising argon bubbles reaching the surface of the molten aluminium alloy and rupturing immediately in an argon-filled hemisphere formed previously. Figure 10 shows individual images of this movie, which is recorded with the fastest achievable frame rate using the microfocus X-ray tube (4 fps). Alloy AlSi9Mg0.6/SiC/20p is processed at 680 °C. Movie displays foaming in real time as given on bottom right.

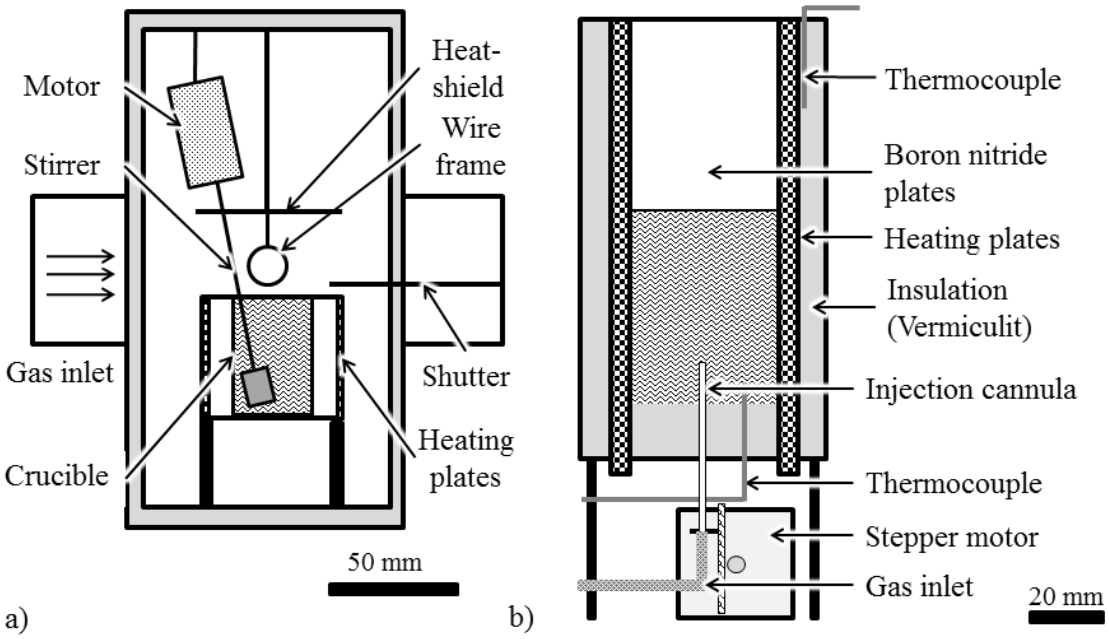

Figure 1. a) Schematic cross section of the film pulling set-up featuring the heated crucible and the stirring and film pulling devices. b) Gas injection furnace with moveable injection cannula used for the foaming experiments.

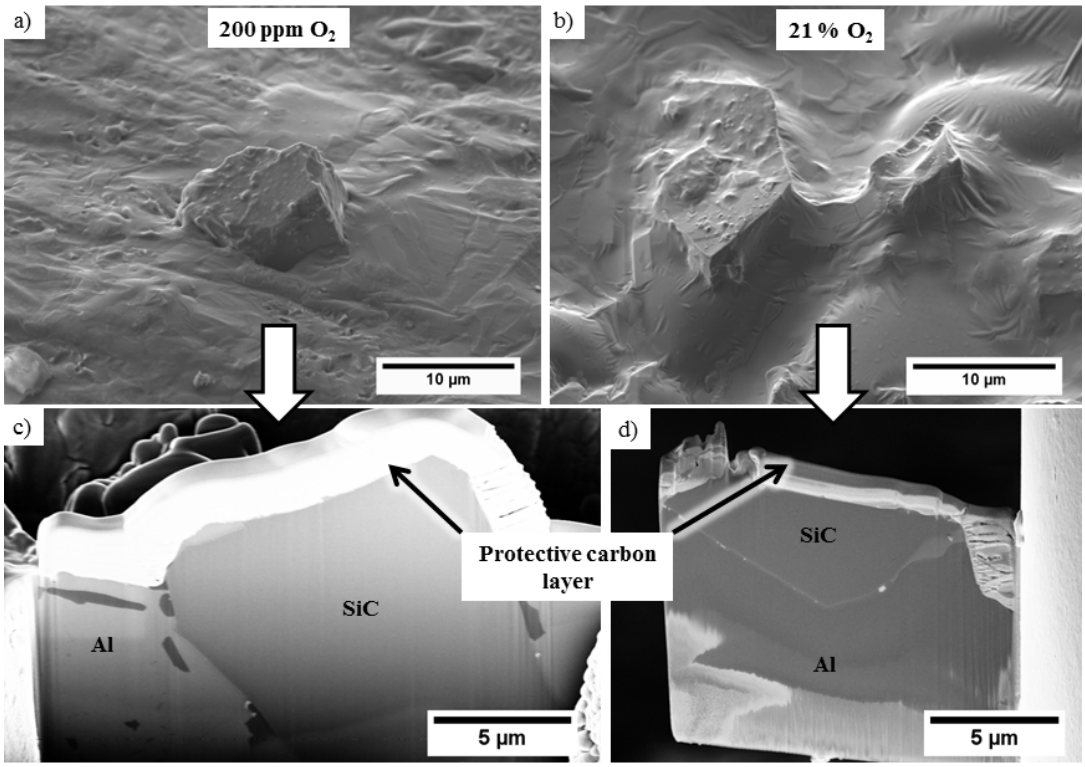

Figure 2. SEM image (taken with the secondary electron (SE2) detector) of SiC particles at the surface of an AlSi9Mg0.6/SiC/20p film drawn in an atmosphere containing a) 200 ppm and b) 21 % oxygen. c,d) corresponding cross sections captured with the in-lens detector during the preparation of TEM samples using a focussed ion beam.

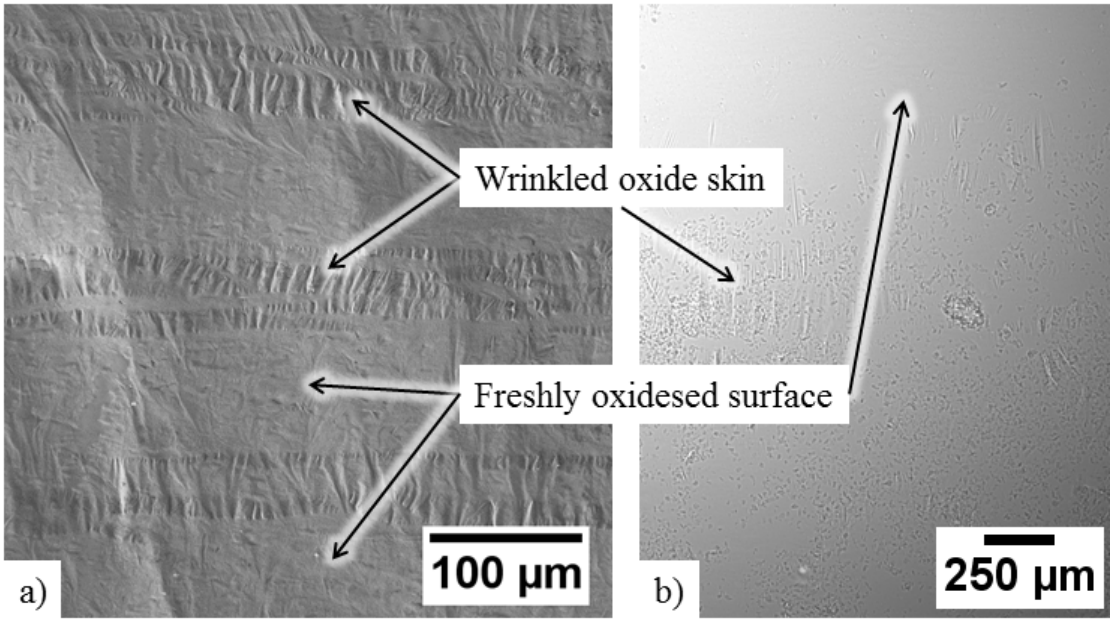

Figure 3. Wrinkled and ruptured oxide skin on the freshly oxidised surface of an AlSi9Mg0.6/SiC/20p film pulled in air. a) SEM image (taken with the secondary electron (SE2) detector) of a sample made using the SF model and solidified immediately after pulling. b) Synchrotron X-ray radiography taken in the liquid state of another sample of the same material. Film made by pulling the QPF model out of a melt at 680 °C.

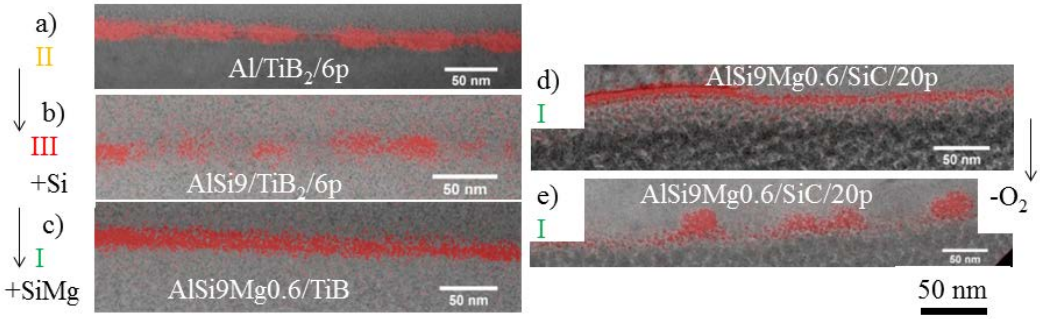

Figure 4. Overlay of TEM bright-field images with oxygen-sensitive EFTEM images (red spots indicate oxygen in oxides) showing the solid-gas interface of a single film (SF, solidified within 10 s) pulled in an atmosphere containing 21% O_2 (a-d) or at 1000 ppm oxygen partial pressure (e). Various systems are investigated: a) Al/TiB_2/6p, b) AlSi9/TiB_2/6p, c) AlSi9Mg0.6/TiB_2/6p and d,e) AlSi9Mg0.6/SiC/20p. The side of the alloy is the one with the composition label. Roman numerals denote whether a film is stable (I), semistable, i.e. stable for small wire frame diameters only (II) or unstable (III).

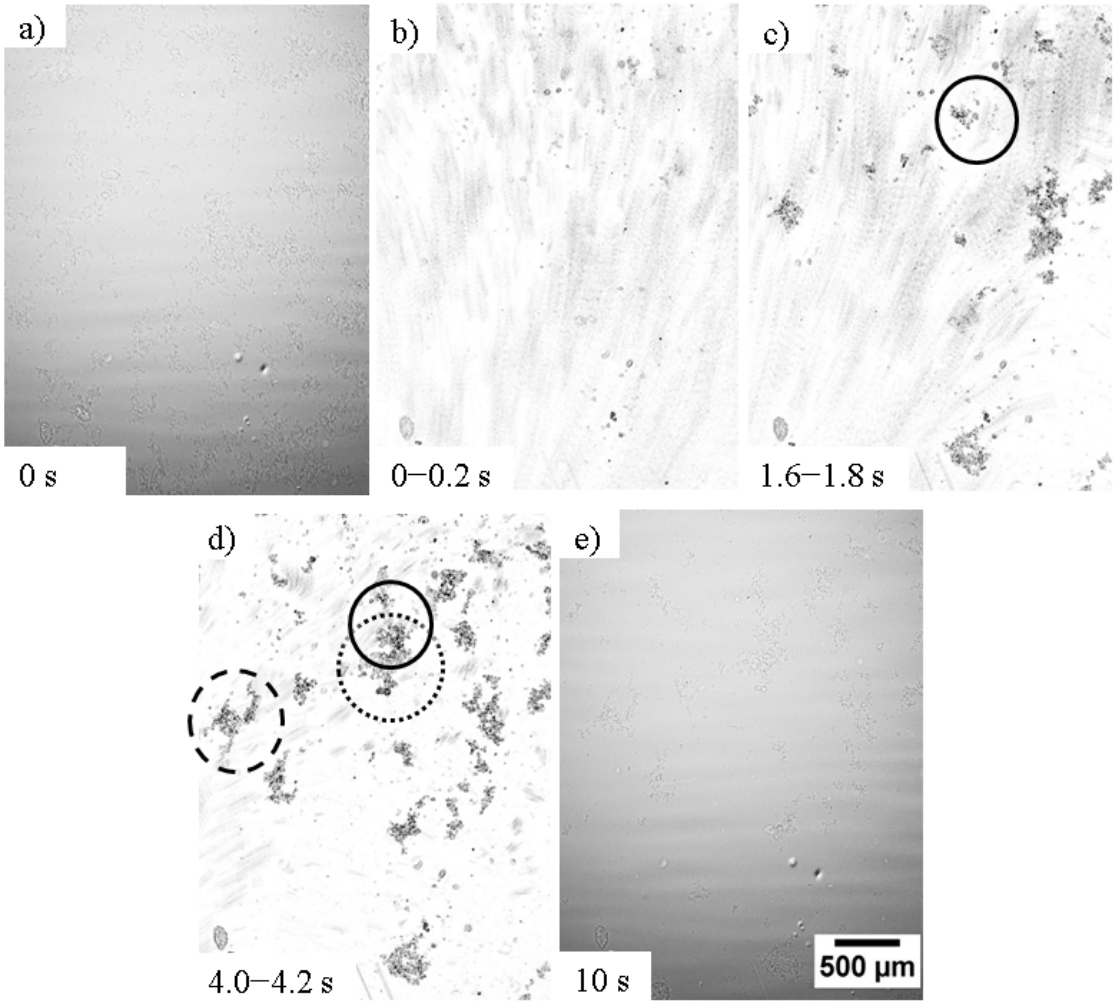

Figure 5. Synchrotron X-ray radiographies (E = 19 keV) of an AlSi9Mg0.6/SiC/20p film pulled in air at 680 °C. a) single image of the state immediately after the end of pulling when the liquid film has come to a rest, b) after integrating over the first 0.2 s and image processing, c,d) same as b) but integrated image 1.7 s or 4.1 s after pulling, respectively. e) shows again the final raw radioscopy 10 s after pulling. Dark blurred vertical stripes indicate particles in motion. Sharp, clearly recognisable spots represent individual particles or particle clusters originally in motion but now immobile and at a fixed position (type 3). Solid circle in c) marks such an exemplary immobilised particle, to which in d) a further cluster attaches (broken circle). The horizontal stripes in a) and e) are caused by fluctuations of the beam and not by the sample. The phenomena discussed in this figure can be seen in real time in supplementary Movie 1.

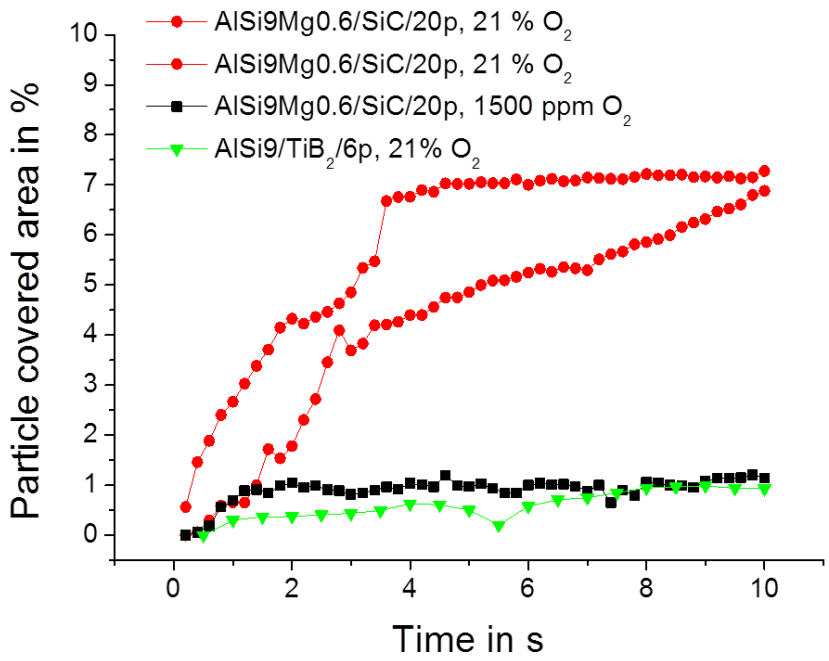

Figure 6. Analysis of films pulled with the QPF model. Area within the FOV in film covered with particle clusters that are first mobile and then fixed (type 3) and have each more than 1000 µm² area, expressed as a fraction of the total area of the FOV. Three combinations of material and oxygen concentration are investigated. In one case an experiment is duplicated.

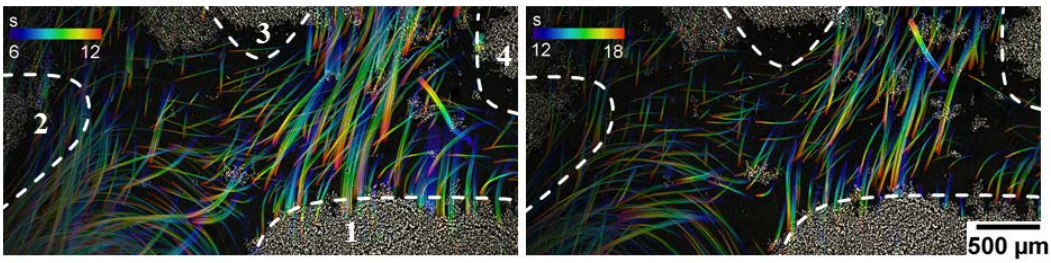

Figure 7. SiC particle trajectories (type 1+3) in a AlSi9Mg0.6/SiC/20p film pulled in air from a melt at 680 °C. This visualisation is obtained by image processing, particle tracking and temporal integration over 6 s of a series of synchrotron X-ray radiographies taken at 19 keV energy. The colour scale defines particle positions at a given time (in seconds) shown in the period a) 6–12 s and b) 12–18 s after pulling. White broken lines denote boundaries between free melt and already fixed immobile clusters (type 2 + 3) appearing as white spots. '1' marks a region where particles flow into an already fixed cluster, regions '2−4', where no particles emerge from inside, behind or in front of the clusters. Movie 2 provides an impression how particles move through this structure in real time.

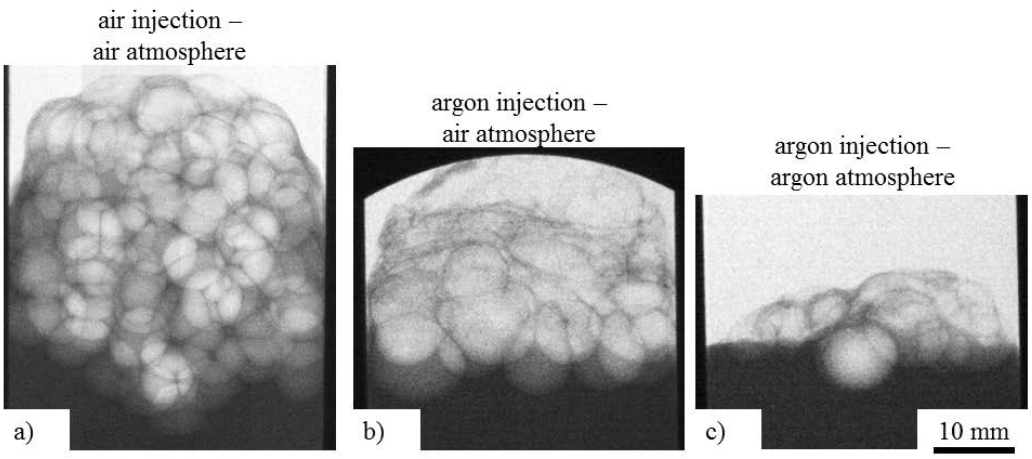

Figure 8. X-ray radioscopies of AlSi9Mg0.6/SiC/10p foam blown by injecting a) air or b) argon. Both foams are surrounded by air. c) Argon is injected and foam is surrounded by Ar atmosphere. The images are taken after stopping bubbling and holding at 680 °C for 600 s.

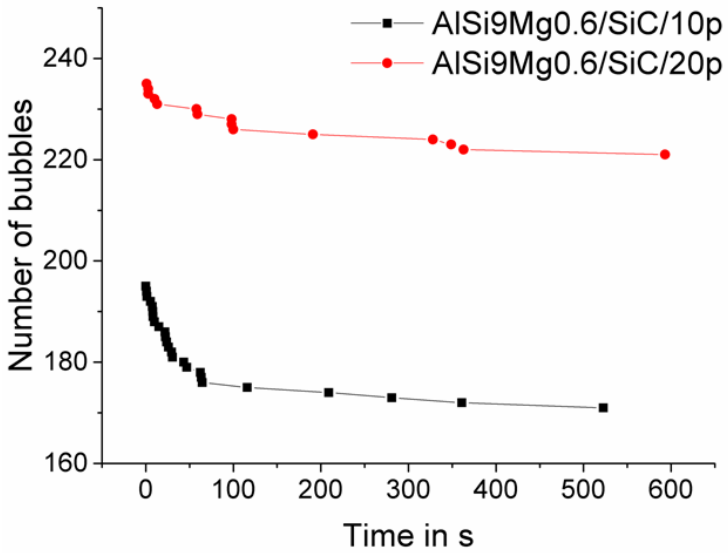

Figure 9. Number of bubbles left after holding for a given time at 680 °C after foams have been created by bubbling argon into AlSi9Mg0.6/SiC/10p or AlSi9Mg0.6/SiC/20p melts for 15 s. The melt is surrounded by air.

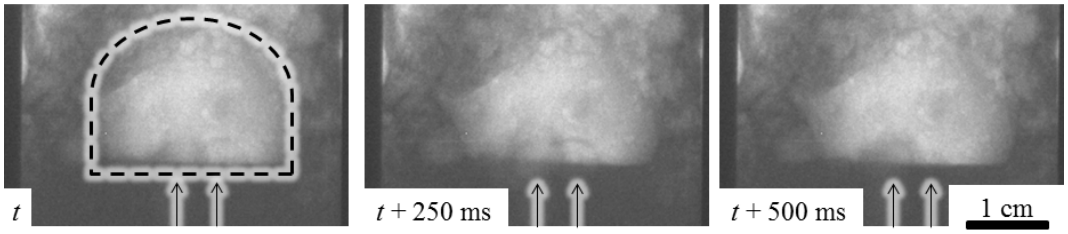

Figure 10. X-Ray radioscopy of ascending bubbles that reach the surface and rupture immediately. The point of interest lies within a large argon filled semisphere produced by a rising argon bubble previously (broken line on left). The arrows show where successive smaller argon bubbles ascend and rupture at the interface to the larger argon-filled volume. Images are recorded every 250 ms. The AlSi9Mg0.6/SiC/20p melt is kept at 680 °C for the experiment. The process of bubble rupture can be followed in real time in supplementary Movie 3.

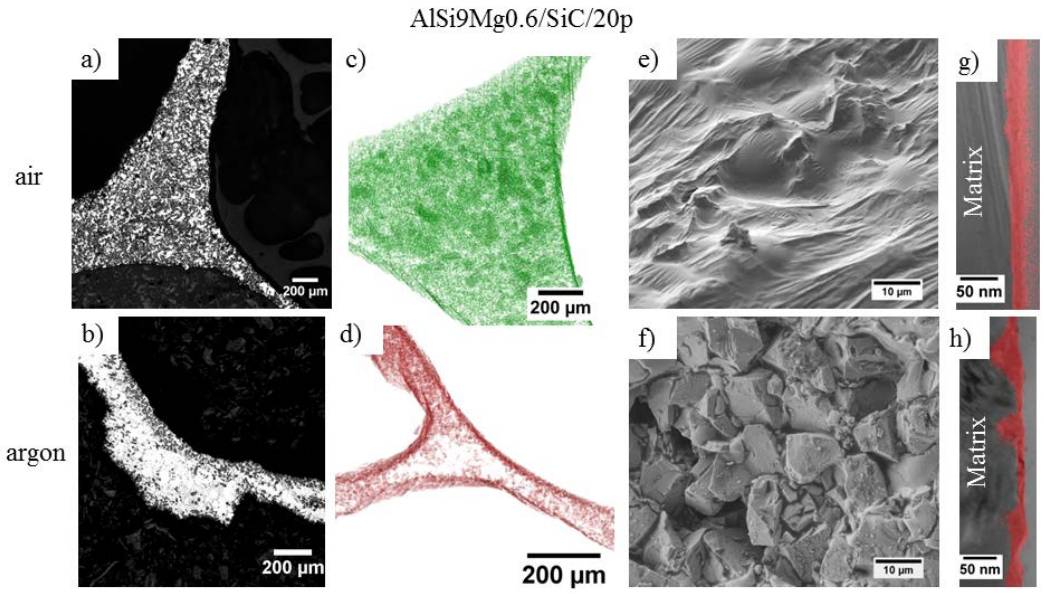

Figure 11. Metallographic cross sections of Plateau borders in AlSi9Mg0.6/SiC/20p foams produced by injecting a) air or b) Ar gas. Synchrotron X-ray tomography of the same foams: c) green spots indicate SiC and their distribution inside a Plateau border; d) red spots indicate SiC particles and their tendency to remain at the solid-gas interface. e,f) SEM images of SiC particles at the inner bubble surface. g,h) overlay of a TEM bright-field image with an oxygen sensitive EFTEM image at the solid-gas interface of the same foam (red spots mark the oxides). ‘Matrix’ indicates the side of the alloy.

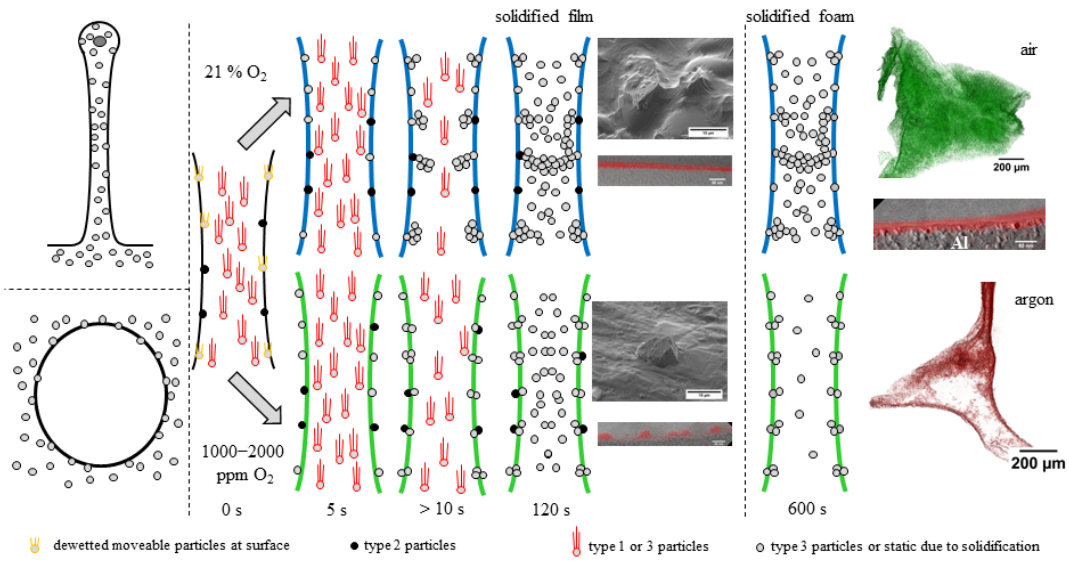

Figure 12. Schematic model of the processes and particle movements in single metallic films and films in foams depending on the oxygen concentration in the environment of the film or in the gas used to blow the foam. Red circles indicate fast flowing particles in the centre of the film, yellow circles are slowly flowing and barely wetted particles at the liquid-gas interfaces, while solid black dots are particles that have been immobile from the very beginning (type 2). Grey circles represent immobilised clusters that have been initially mobile (type 3) or are static due to solidification. The black margins of the film surface (0 s) indicate a direct transition of the liquid to the gaseous phase. The following blue margins mark a continuous oxide skin, in contrast to a surface structure consisting of oxide islands (green margins).

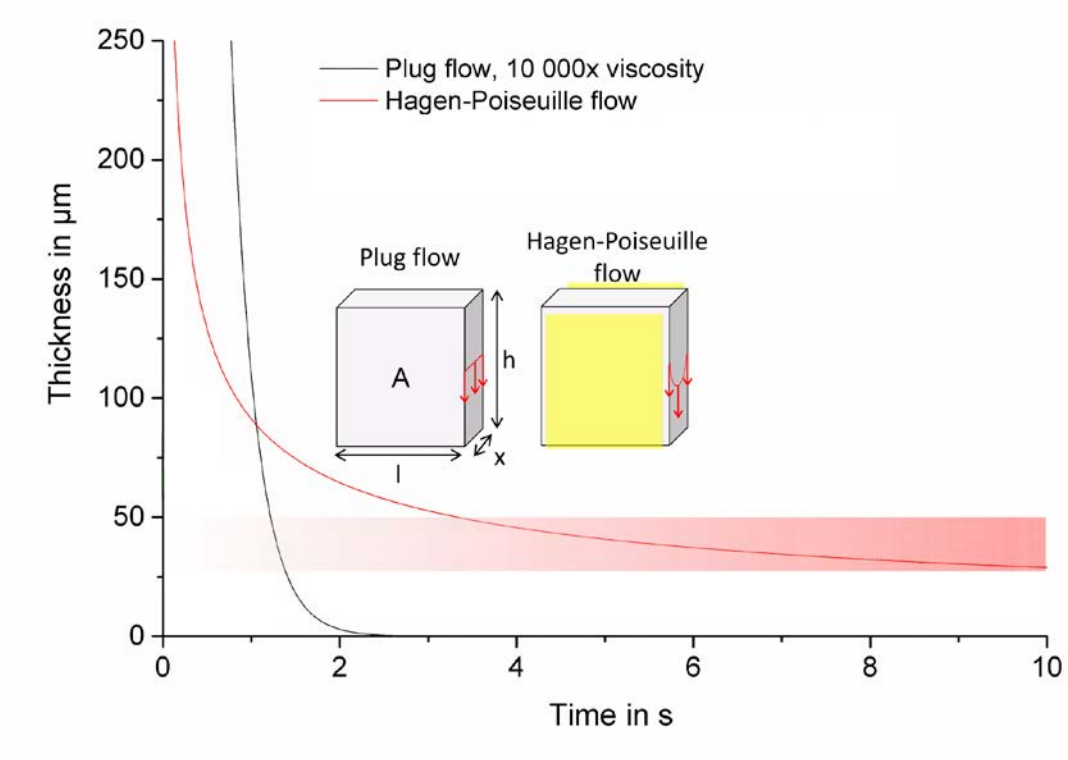

Figure 13. Comparison of the thickness reduction with time of an AlSi9Mg0.6/SiC/20p film governed either by gravity-driven plug flow (viscosity increased × 10^4) or Hagen-Poiseuille flow (yellow area indicating the immobilising oxide skins) or by capillary-driven flow. The red bar indicates the experimentally determined critical film thickness range in liquid foams.